In-situ Visualization of Flow Mechanisms in Macroporous Soils using 4D X-Ray Computed Tomography

Abdullah Al Mamun[1], Mine Dogan[3], Brian A. Powell[1†], Timothy A. DeVol[1†], Stephen M. J. Moysey[1,2]

[1]Environmental Engineering and Earth Science Department, Clemson University, Clemson, SC 29634, USA.

[2]Department of Geological Sciences, East Carolina University, Greenville, NC 27858, USA.

[3]Department of Geological and Environmental Sciences, Western Michigan University, Kalamazoo, MI 49008, USA.

[†]Center for Nuclear Environmental Engineering Sciences and Radioactive Waste Management, Clemson University, Clemson, SC 29634-0942, USA.

Corresponding author: Abdullah Al Mamun (abdullm@g.clemson.edu)

Key Points:

- Different macropore flow mechanisms were observed using 3D time-lapse high-resolution Computed Tomography (CT) imaging.
- Water content from CT images was determined using a method that doesn't require any image thresholding or spatial porosity distribution.
- Interactions between macropores and the soil matrix were observed to produce complexly connected flow networks.

Abstract

Transfer of mass between macropores and the soil matrix is an important control on flow and solute transport in the vadose zone. Few empirical techniques are available to explicitly investigate how the fast flows in macropores interact with the slower flows in the matrix to allow the flow system to evolve over time. In this study, time-lapse X-ray Computed Tomography (CT) scans are used to obtain quantitative 4D (i.e., transient three-dimensional) images of infiltration in two soil columns: one homogenous, non-macroporous and one containing a network of desiccation cracks. Water was applied to the top of each column at increasing rates over the flow period. High resolution (80 micron) CT images of the columns were collected throughout the infiltration experiments at 7-minute intervals. These images were processed to obtain time-varying maps of water content that provide insights to the evolution of the flow patterns and mechanisms of interaction between the macropore and matrix domains. Flow in the non-macroporous column was observed to be nearly uniform, whereas flow behavior in the macroporous column was dependent on the influent water flux. At low infiltration rates, film flow occurred in the macropores with comparatively little imbibition from macropore to matrix. At high infiltration rates, the macropores filled with water and imbibition to the matrix increased. Results demonstrate that wetting of the soil is a complex process reflecting contributions from downward infiltration through macropore-matrix networks and lateral wetting from the macropores.

1 Introduction

The importance of fast flow and transport through soil macropores has been recognized since 1864 with interest growing substantially over the last 35 years due, in particular, to water quality impacts associated with agricultural discharge (Beven & Germann, 1982; Beven & Germann, 2013). Macropore flow occurs in large, continuous voids, such as root channels, fissures, earthworm burrows, or cracks. Jarvis (2007) suggested that pores of 'equivalent cylindrical diameter' greater than about 0.3–0.5 mm (i.e., water- entry pressures of –10 to –6 cm H_2O in the Laplace equation) can be classified as a macropore, but there is currently no widely accepted definition for macropores. Regardless, macropores are ubiquitous and often viewed as the most frequent cause of preferential flow in field soils (Jarvis et al., 2016). Flow through macropores can capture large fractions of the total volume of flow through a soil, causing most of the soil matrix to be by-passed and remain dry.

Ponded conditions generated from a heavy rainfall event, high irrigation rates, or surface depressions can allow water to enter macropores that extend to the soil surface, thereby producing high transmission rates through the soil profile (Beven & Germann, 1982; Iqbal, 1999; Weiler & Naef, 2003). In addition, water flowing through the soil matrix can also enter a macropore when the water pressure on the macropore-matrix interface exceeds the 'water-entry' pressure of macropore. This generally occurs when a portion of the soil matrix comes close to or reaches saturation (Hendrickx & Flury, 2001). Once water gets into the macropore, a small increase in soil water pressure leads to a rapid increase in water flow rate due to the sharp contrast in pore size and tortuosity compared to the surrounding matrix pores (Jarvis, 2007).

The flow mechanisms contributing to the configuration, geometry, and degree of saturation of water in individual macropores and the soil matrix are thought to be controlled by a balance between the supply of water to the macropore and losses from the macropore due to imbibition by the matrix (Jarvis, 2007). At low saturation and flow rate, film or rivulet flow occurs along the

walls of the macropore (Dragila & Wheatcraft, 2001; Tokunaga & Wan, 1997). If the net flow rate is increased, films or droplets can connect locally across the void of the pore space to form a capillary bridge, particularly at regions where the macropore width varies (Bouma & Dekker, 1978; Wang & Narasimhan, 1985). These liquid clusters may migrate down the macropore or grow until they become destabilized, at which point water may sweep down the macropore to produce an intermittent or pulse flow (Germann et al., 1987; Ghezzehei & Or, 2005; Gjettermann et al., 2004). It is rare that all macropores in the soil are full of water under unsaturated flow conditions as only a portion of them form continuous pathways to the inflow and due to the presence of pore 'necks', dead-ends or isolated pores (Bouma et al., 1977; Perret et al., 1999). A simplified demonstration of these mechanisms is presented in Figure 1.

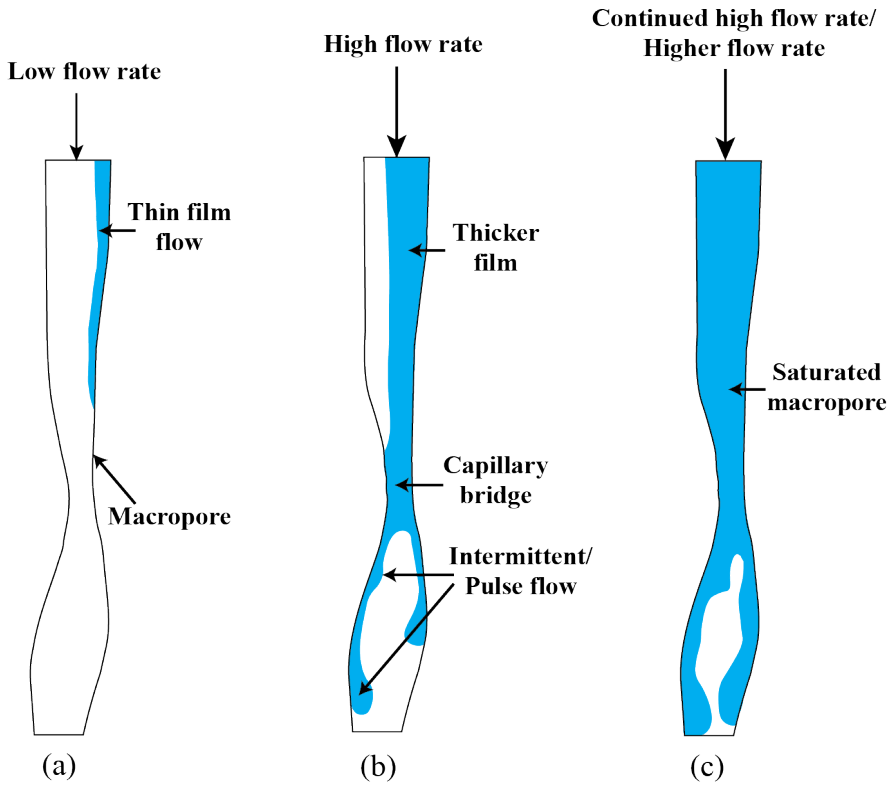

Figure 1. Mechanisms of macropore flow: (a) Film flow; (b) Capillary bridging and Intermittent/Pulse flow; (c) Saturated macropore

Destructive methods of investigation involving the excavation of a soil to identify flow paths marked by dye tracers have been a common approach used to study preferential and macropore flow through soils in the past (Flury & Wai, 2003; Beven & Germann, 2013). Breakthrough curves derived by collecting leachate from gravity-flow or from soils placed under capillary suction have also been used as an indirect means to understand solute transport driven by preferential flow (Hangen et al., 2005; Schmidt & Lin, 2007). However, these methods are unable to offer detailed information regarding the mechanisms of macropore-matrix interaction or the evolution of flow pathways in the soil over time. Artificial macropores and idealized physical models have been used to visually study the mechanics of flow in macropores (e.g., Dragila & Weisbrod, 2004; Ghezzehei & Or, 2005), but are not fully representative of real soils. In contrast, non-invasive, three-dimensional (3D) imaging techniques have become important tools in subsurface flow and

transport research as they permit nondestructive examination of in-situ soil structures and flow processes (Binley et al., 2015; Gantzer & Anderson, 2002; Perret et al., 1999; Warner et al., 1989; Werth et al., 2010). Among all the imaging techniques, X-ray Computed Tomography (CT) has been especially useful for studying macropores because of its high spatial resolution and sensitivity to water, air, and solids (Kalender, 2005; Ketcham & Carlson, 2001; Mees et al., 2003) that allow for mapping of soil structures (i.e. root network, pore network, cracks etc.) as well as monitoring dynamic processes within the soil, such as root development, water flow, and solute transport (Capowiez et al., 2014; Koestel & Larsbo, 2014; Luo & Lin, 2009; Mooney, 2002; Sammartino et al., 2015; Tippkötter et al., 2009; Tracy et al., 2015; Weller et al., 2018).

A limited number of past studies have used X-ray CT imaging to determine the spatial distribution of water or tracers in the soil relative to structural features. For example, Mooney (2002) used image segmentation based on thresholding to separate air filled porosity and water filled porosity in order to evaluate the relationship between water distribution and soil macropores for CT images taken before and after an infiltration event. Luo et al. (2008) performed real-time CT imaging of the movement of a potassium iodide tracer through a saturated soil column to determine that interactions between macropores and the soil matrix were complex, with only a subset of connected macropores contributing to transport processes. Sammartino et al. (2015) used a novel thresholding and frequency analysis of real-time CT data collected with a coarse spatial resolution (i.e., 332 μm) to identify preferential flow pathways formed over the course of an infiltration experiment. Though the CT resolution was not sufficient for direct imaging of macropore processes and the analysis method was not able to produce estimates of water content in the soil matrix, these authors were able to compare their CT results against a dye tracer to show good agreement between the two methodologies and to confirm that only a small portion of the macropore network contributed to unsaturated flow. Weller et al. (2018) improved on these results to provide quantitative time-lapse images of water content changes during infiltration in various soil columns, though macropores were not a focus of that effort.

In this study we utilize time-lapse X-ray CT imaging to investigate the mechanisms of flow that occur within macropores and the interactions between macropores and the soil matrix that occur during an infiltration event. The focus here is on linear macropores formed as desiccation cracks, rather than the long-linear biopores (e.g., root channels) that are the focus of most previous studies. We use a high-resolution, pre-clinical VECTor^{4}CT instrument that allows the soil column to remain vertical in the scanning bed throughout the experiment. In addition to imaging the movement of water in the macropores, we also determine pixel-by-pixel volumetric water content estimates over time throughout the column.

2 Materials and Methods

2.1 Soil Sample Preparation

The soil used in this experiment was collected from the Savannah River Site (SRS), South Carolina. The SRS soil has a pH of 4.8, infield dry bulk density of 1.66 g/cm^3, saturated hydraulic conductivity of 3.38 x 10^{-4} cm/sec and surface area of 14.1 m^2/g as measured by N_2 adsorption (Micrometrics ASAP 2000 Surface Area Analyzer) (Dogan et al., 2017). Two different packing methods were used to prepare a homogenous and a macroporous soil sample in separate polycarbonate columns (1.5-inch diameter and 6-inch length) in preparation for the subsequent

infiltration experiments. The bottom of each polycarbonate tube was sealed by a grooved PVC cap and a filter paper (particle retention of 1 μm) to allow free outflow from the column during the infiltration experiments. To prepare the non-macroporous column, the SRS soil was packed with an initial gravimetric water content of 12.5% following the procedure for the calibrated standard Proctor method (ASTM D698) in terms of the number of compacting layers, number of blows per layer, hammer weight, and drop of hammer, to obtain a final compacting effort of 12400 lb-ft/ft^3. The macroporous column was initially packed at near saturation with 37% initial gravimetric water. Soil was added to the column in five stages, between which vibration was used to settle the soil with 25 blows of the bottom of the column against a solid surface from 2 cm dropping height. The top of the both columns were then left open, letting them to dry over a period of 2 months to allow desiccation. The loss of moisture and resulting shrinkage slightly reduced the packing height of 6 inch for both columns at the end of the drying period.

2.2 Experimental Setup

The experimental setup for the infiltration tests is shown in Figure 2. A 1M NaI solution was used for the influent to ensure that the water infiltrating the column could be readily viewed in x-ray CT images obtained during the experiments (Clausnitzer & Hopmans, 2000). We assume that the NaI is conservative and representative of the flow of water. Water was added to the center of the soil surface at the top of the column drip irrigation using a peristaltic pump. The non-macroporous column was subjected to three low flow rates (i.e. 0.058 mL/min for 0-180 minutes, 0.086 mL/min

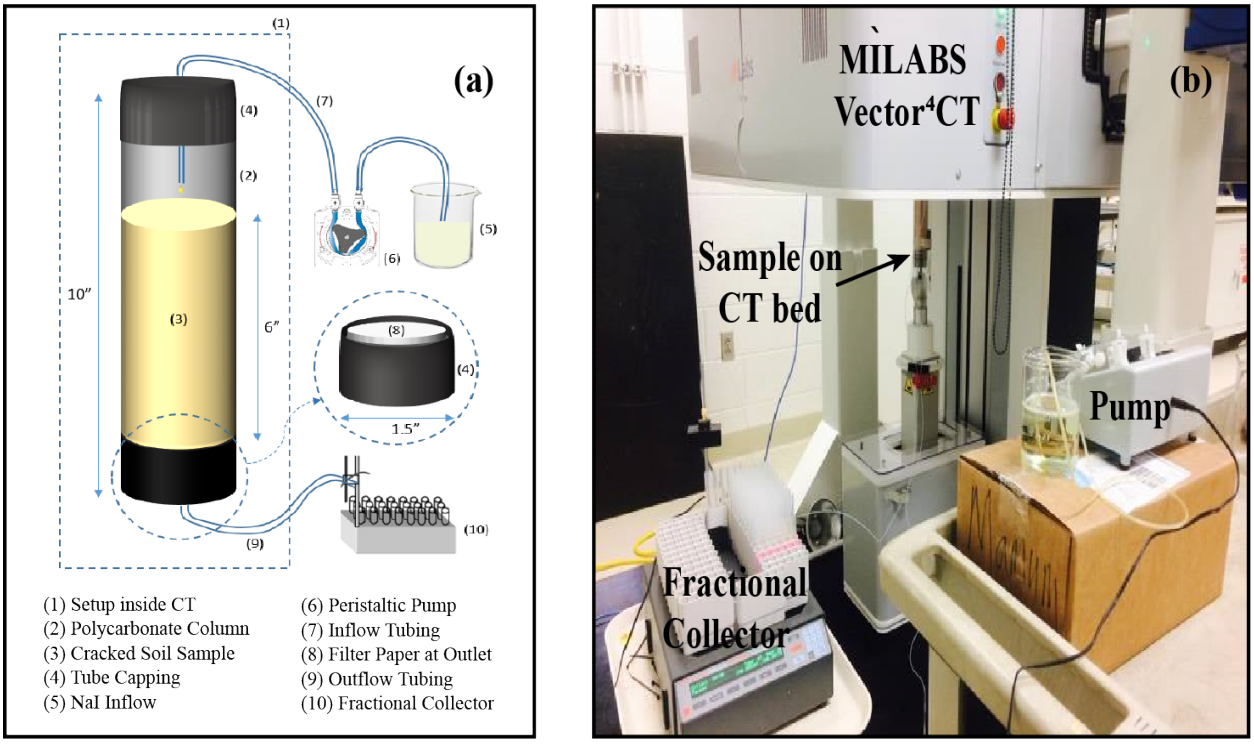

Figure 2. Experimental setup showing (a) schematic of the column apparatus and (b) the column placed vertically in the bed of the CT scanner.

for 180-420 minutes and 0.116 mL/min for 420-660 minutes) over a period of 11 hours. Then the flow was stopped for a period of 12 hours and again resumed with a higher flow rate of 0.4 mL/min for one hour before terminating the experiment. For the macroporous column, three different flow

rates (i.e. 0.058 mL/min for 0-90 minutes, 0.116 mL/min for 90-420 minutes and 0.33 mL/min for 420-480 minutes) were used during the entire infiltration experiment. The purpose of these inflow rate changes for both experiments was to observe the flow behavior responses. An automated fraction collector was used to collect the outflow in every 30 minutes through an outlet tubing.

The infiltration experiments were performed while the column was secured within the bed of a high-resolution VECTor^{4}CT instrument (MILabs, The Netherlands) that was customized to allow for a vertical column placement. The scan parameters were kept fixed for each of the scans taken during the experiment. The x-ray tube voltage and current were maintained at of 55 keV and 0.37 mA, respectively. Each scan took around 7 minutes to complete and during this time the CT scanner generated a total of 1440 2D slices (i.e., 3 sub-scenes; 480 rotations per sub-scene; 1-2D slice per rotation) and 1896 2D slices (i.e., 3 sub-scenes; 632 rotations per sub-scene; 1 2D slice per rotation) for the non-macroporous and macroporous soil columns, respectively. A total of 90 scans and 65 scans were taken for the non-macroporous and macroporous soil columns during the infiltration experiments including the dry scans before starting the pump. To be consistent in terms of orientation and alignment of the reconstructed CT images, the soil columns were never removed from the CT bed until the completion of the experiment. Finally, all the scanned images (i.e., 2D slices) were reconstructed into 3D images at a resolution of 80 microns (i.e. voxel size = 0.08 mm x 0.08 mm x 0.08 mm).

2.3 Data Analysis

2.3.1 Pre-Processing and Noise Reduction

Each of the reconstructed images was subjected to several preprocessing steps using the software ImageJ (i.e., *Crop, Clear outside* and *Make substack*) (Abràmoff et al., 2004) in order to remove the image background and polycarbonate tube (i.e. the resulting image only consists of macropores and soil solids). Noise reduction was performed to attain better accuracy from pixel by pixel water content calculations. A moving average filter with window size of 11 by 11 pixels was applied in each scan for smoothing based on the calculated optimal sum of absolute difference (SAD) in terms of CT intensity value between raw image pixels and corresponding smoothed image pixels.

2.3.2 Calibration of NaI and Air

A scan of 1M NaI solution alone was performed in a 1.5 in diameter polycarbonate tube with the same scan parameters as for the soil. The resulting pixel intensities showed a radial dependence (i.e., higher intensities around the column edges and lower intensities at the center) due to partial volume effect (Barrett & Keat, 2004), which is a CT imaging artifact. A correction for this effect was developed by fitting a polynomial model to the radial intensity trend (Eq. 1).

$$CT_{NaI} = -331.1708 - 0.0031 * R^{2.5} + 0.00026 * R^3 \quad (1)$$

Where, CT_s = the CT Number for component '*s*' (i.e., soil, air, water, NaI solution) in Hounsfield Unit (HU) $= \frac{\mu_s - \mu_{water}}{\mu_{water} - \mu_{air}} \times 1000$

μ_s = linear attenuation coefficient of component '*s*'

R = Radial pixel distance from the center pixel in 2D XY plane $= \sqrt{X^2 + Y^2}$; $r^2 = 0.93$

Also, the CT Number of air was calibrated by calculating the average intensity over an empty region, which resulted in a value of -999.84.

2.3.3 Water Content Calculation

The water content for a pixel located at coordinates (*x,y,z*) in an image scan collected at time *t* was calculated using a volumetric mixing model in terms of CT number (Eq. 2), similar to the approach used by Luo et al. (2008):

$$\begin{aligned} CT(x,y,z,t) &= CT_{Solid}(x,y,z)*[1-\varphi(x,y,z)]+ \\ CT_{NaI}(x,y,z)*\varphi(x,y,z) &* S_{NaI}(x,y,z,t)+CT_{Air}*\varphi(x,y,z) * S_{Air}(x,y,z,t) \end{aligned} \quad (2)$$

Where, $\varphi =$ pixel porosity, $S =$ water saturation, and the subscripts again refer to the mineral grains (*Solid*), void space (*Air*), and infiltrating solution (*NaI*). The CT numbers of the solid, air, and NaI solution represent values for a non-macroporous material, thus are constant through time. Changes to the CT number of a given pixel through time are therefore the direct result of changes in water saturation. For the initial scan of the soil before the onset of infiltration, we assume that the soil is dry, such that $S_{NaI}=0$ and $S_{Air}=1$.

In this case, Eq. (2) can be rearranged to obtain:

$$CT_{Dry\_scan}(x,y,z)=CT_{Solid}*(1-\varphi(x,y,z))+CT_{Air}*\varphi(x,y,z) \quad (3)$$

For the scan during infiltration at time t: $S_{Air}(x,y,z,t)=1-S_{NaI}(x,y,z,t)$

Substituting $\varphi(x,y,z)*S_{NaI}(x,y,z,t)=\theta(x,y,z,t)$ and Eq. (3) into Eq. (2), we finally get,

$$\theta(x,y,z,t)=\frac{CT(x,y,z,t)-CT_{Dry\_scan}(x,y,z)}{CT_{NaI}(x,y,z)-CT_{Air}} \quad (4)$$

where, $\theta =$ volumetric water content

Eq. (4) allows for the calculation of water content for each pixel for a specific time t. $CT(x,y,z,t)$ and $CT_{Dry\_scan}(x,y,z)$ were obtained from the scans obtained during the infiltration experiment at time t and the initial dry scan, respectively. Note that these values intrinsically account for spatial variability in porosity, thus it need not be assumed that the porosity is constant or known. $CT_{NaI}(x,y,z)$ and CT_{Air} were obtained from the calibration with scans of the pure solution and air as described earlier.

2.3.4 Water Content Validation:

It is not possible to independently validate water content estimates at the pixel scale. Therefore, to validate the water content values obtained by applying the model given in Eq. 4, the actual average volumetric water content of the column over time determined from the known cumulative inflow (with no outflow) is compared to that derived from the CT images collected at different times over the course of the experiment (Fig. 3). This comparison shows a good correlation and quantitative agreement for the lowest and highest flow rate periods (i.e., first 1.5 hours and last 1 hour) for the

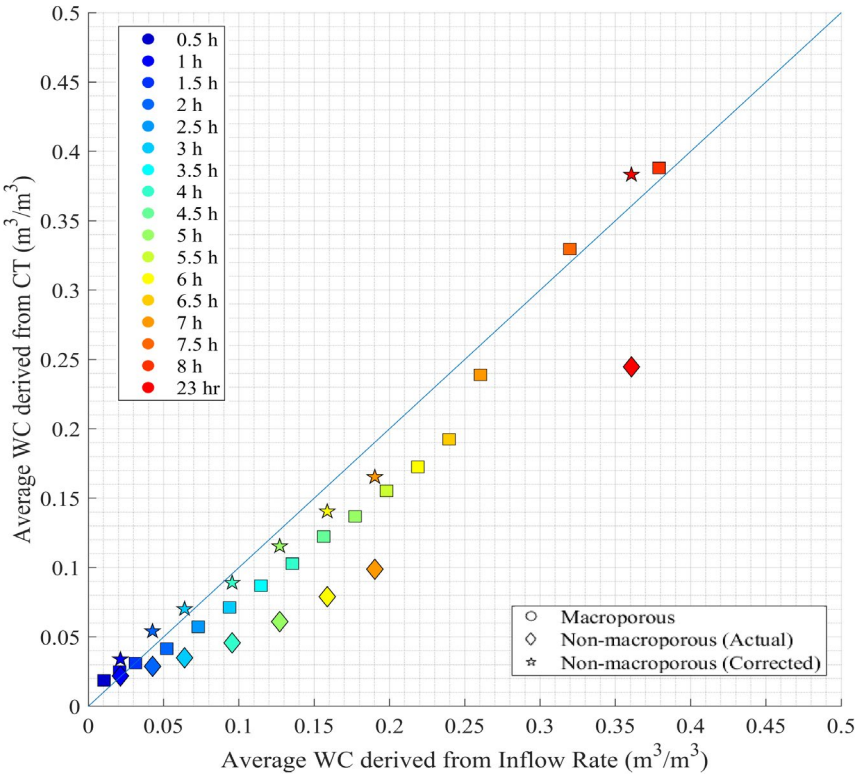

Figure 3. Validation of the water content estimates performed by comparing the average water content of the column derived from the cumulative flow introduced to the column versus averaging the water content estimates from the time-lapse CT scans. The color scale reflects time since the initiation of infiltration. The square shaped data points represent macroporous column; diamond and star shapes represent uncorrected and corrected data set for non-macroporous column respectively.

macroporous column. In the middle of the experiment, however, the net inflow volume estimated by the CT scans underestimates the average volumetric water content of the column by up to 5% (vol./vol.) for the macroporous column and by over 10% (vol./vol.) for the non-macroporous column. The underestimation in the case of the non-macroporous column may result from a shadow region apparent near the top of the column in the CT images. We interpret this effect to potentially be caused by shielding associated with high concentrations of NaI at the source of the infiltrating water. The low apparent water contents in this region are corrected by assuming that the CT intensity should be equivalent to that observed in other saturated areas of the non-macroporous column. The agreement between the average water contents derived from the net inflows versus the corrected CT estimates are then within 3% (vol./vol.) (Fig. 3). A similar shadow zone is observed for the macroporous column, however, due to the nature of the heterogeneous flow it is less likely that the shielding effect would have occurred in this region and similar corrections are therefore not applied in this case. Though the errors in water content at the pixel scale are likely to be larger than for the average water contents shown in Figure 3 due to local noise in the image, these values give a first order estimate of a representative value of the average water content error for the imaging experiment (i.e., <5%) and confidence in the quantitative estimates of the water content.

3 Results

3.1 Macropore Network

Representative slices through the three-dimensional CT scans of the two soil columns are shown in Figure 4. No macropores were found in the homogeneous soil packed using the Proctor method, whereas multiple macropores were present in the other column. As shown in Figure 4b, the macropore network consists of one primary crack extending from the bottom of the column, where it is located near the center, to the top of the column, where it is located near the column edge. The crack is a curvilinear, three-dimensional feature and thus cuts through the column in geometrically complex ways as it dips from top to bottom. It is also important to note that the overall macropore network is not a single continuous feature. For example, several other lateral cracks offshoot from

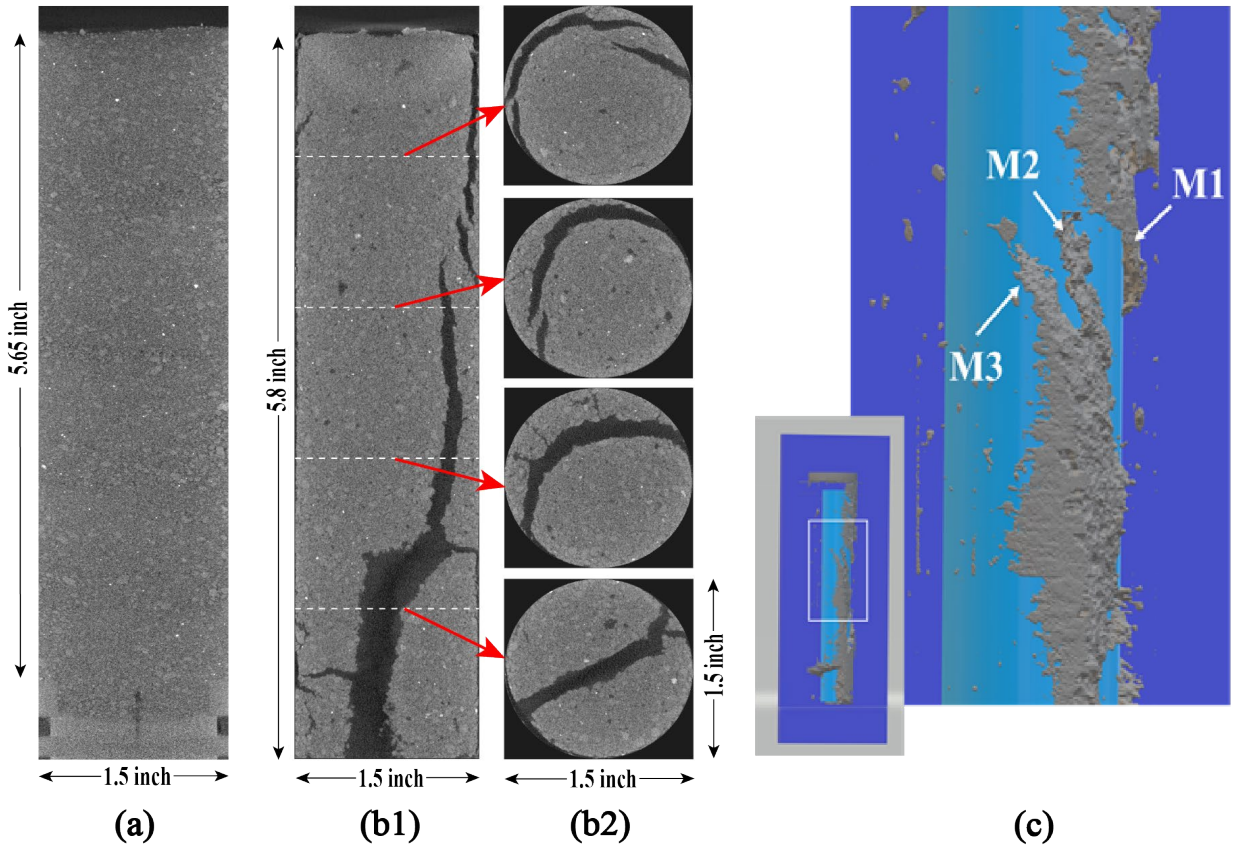

Figure 4. CT images of the soil columns after 2 months of drying: (a) No macropores formed in the soil packed using the Proctor method; (b1) A substantial macropore network formed in the column packed at high water contents. A single desiccation crack dominates the network from the bottom of the column to near the top; (b2) Supplementary cross-sectional views of macropores at four different column heights; (c) The overall macropore network also contains multiple cracks partially disconnected from the main channel, such as those labelled as M1, M2, and M3 in the figure (note, the inner blue cylinder is to aid visualization of the cracks and not a feature of the column).

the primary desiccation crack in Figure 4b. The isosurface rendering in Figure 4c further illustrates how distinct smaller cracks (M1, M2, M3) that are not connected to the primary crack in large portions of the column contribute to the overall macroporosity.

3.2 Infiltration Experiment: Non-macroporous Column

The infiltration experiment in the non-macroporous column was performed as a reference against which to compare the results from the column with the macropore network. The raw time lapse CT images are shown in Figure 5 and water content images obtained from Eq. 4 are shown in Figure 6. Note that the raw CT images are contrast enhanced for better visualization and any inconsistency in grayscale brightness level results from enhancement irregularity. An approximately uniform flow front was observed throughout the course of the experiment (Fig. 5, 6). The shadow zone mentioned earlier can be clearly seen as a relatively empty water content region in a downward conical shape at the top of the column (e.g., Fig. 6a, 6b, 6c, 6d, 6e, 6f, 6g, 6h, 6j); there is no clear hydrologic explanation for this feature, suggesting that it is an artefact of the imaging experiment.

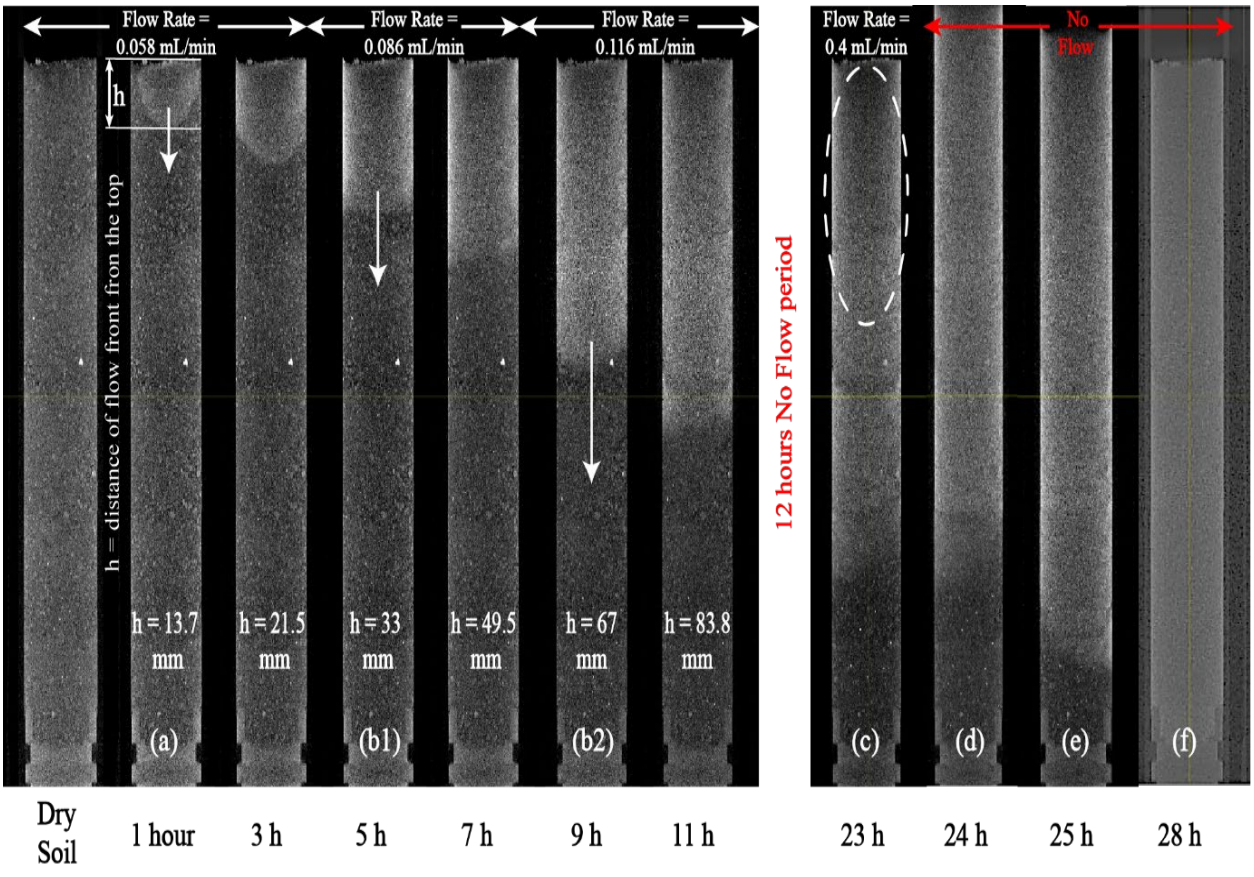

Figure 5: Visualization of flow in the non-macroporous soil column (brighter grayscale represents higher water content): (a) initial flow front, (b) increase in downward rate of flow front advancement with increasing flow rate, (c) water content redistribution after 12 hour period where inflow to the column flow was stopped; saturation at the top of the column decreased in area indicated by oval shape, (d) 1.3 cm ponding at high flow rate, (e) 0.6 cm ponding depth (f) final fluid distribution following infiltration of all ponded water.

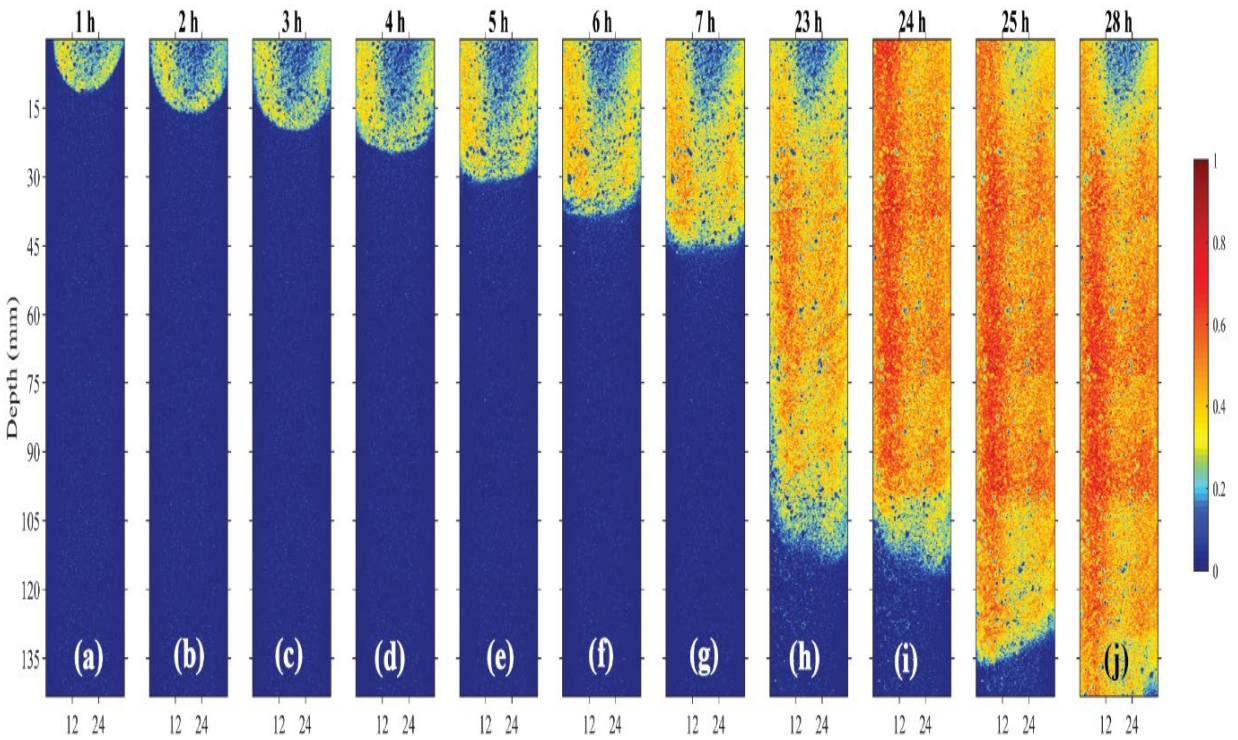

Figure 6. Water content distribution in a vertical slice at the middle of the non-macroporous column. Images couldn't be produced in between 7h and 11h because of two different sets of CT acquisition parameter caused by a CT malfunction after 7h, which didn't allow for image differencing operation.

The downward migration rate of the flow front was nearly constant under each infiltration condition and increased proportionally when the applied flow rate was increased. After 11 hours of inflow, infiltration was stopped for a 12-hour period during which time redistribution occurred. The redistribution is shown by an apparent decrease in the average saturation (i.e., brightness) at the top of the column and an advance of the flow front by approximately 3 cm during this period even though no water was introduced to the column (Fig. 5c). After this period, infiltration was resumed with a flow rate of 0.4 mL/min for 1 hour. During this final application of water, the flow front did not advance significantly, but the water content in the previously wetted zone increased (Fig. 6i). The applied infiltration rate was greater than the infiltration capacity of the soil and resulted in ponding to a depth of 1.3 cm on the soil surface; note that the ponding is apparent above the column in Figure 5d. After irrigation ceased, the ponding depth reduced to 0.6 cm within an hour (Fig. 5e). After three more hours, the saturation level of the entire column appeared to increase significantly as all the ponded water infiltrated (Fig. 5f, 6j).

3.3 Infiltration Experiment: Cracked Macroporous Column

3.3.1 General Patterns of Flow

The time-lapse water content images given in Figure 7 highlight general flow patterns observed during the infiltration experiment for of a vertical slice of the CT volume obtained 10 mm from the column edge (approximately ¼ of the way through the column). Figure 7a shows that flow was

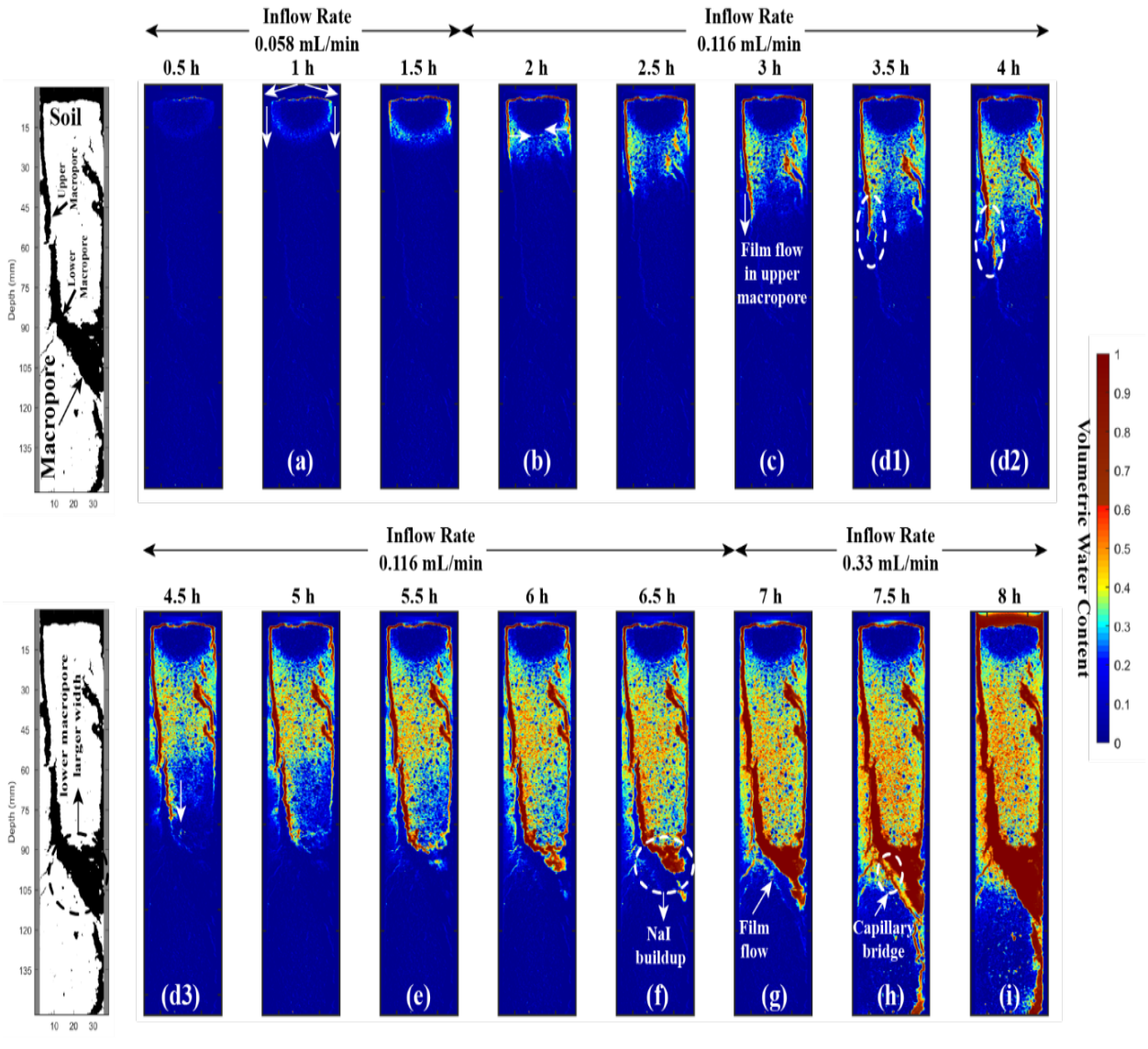

Figure 7. Water content distribution and macropore flow pattern in a vertical slice of the CT volume: (a) flow across the soil surface to macropores at the edge of the column; (b) imbibition from macropores to matrix; (c) film flow in the upper macropore; (d) matrix acting as a bridge between macropores to establish a flow network; (e-f) increasing film thickness along upper macropore surface; (g) film flow on lower boundary; (h) capillary bridging event; (i) saturation of macropores and ponding.

initially redirected across the top of the soil surface from the center, where the irrigation tube was located, toward the edges. A dry zone therefore appears to occur immediately below the soil surface in the center of the column. It was later determined that a crust was present on the soil surface as a result of the packing and drying procedures used to create the macropores, which prevented the solution from directly infiltrating into the soil matrix.

The water running off the soil surface was captured by the macropore network, which at the top of the column primarily consists of a gap formed between the soil and the plexiglass wall that occurs around roughly half of the column perimeter (visible at column edges in Fig. 7). The infiltrating

464 water travelled through this macropore to a depth of about 20 mm in the first hour and a half of
465 the experiment. During this time, water also began to imbibe into the matrix from the macropore.
466 The rate of imbibition appeared to increase once the flow rate was increased to 0.116 mL/min at
467 1.5 hours into the experiment (Fig. 7b). On the right-hand side of the column, the soil matrix comes
468 into contact with the column wall and the macropore closes. Complex wetting behavior is seen in
469 the matrix as water accumulates in this area and eventually downward flow is initiated in a
470 macropore that runs along the column wall. In contrast, the portion of the macropore on the left
471 side of the column migrates inward and is continuous to 60 mm depth where it terminates within
472 the soil. Film flow appears to initiate on the upper surface of this macropore, with the film
473 advancing downward over time until it intercepts the bottom of the macropore at around 3 hours
474 (Fig. 7d1). The matrix wets at the macropore's terminus (Fig. 7d2) and eventually flow is initiated
475 in another, disconnected macropore below (Fig. 7d3). This portion of the matrix between the upper
476 and lower macropores formed an important component of the macropore flow network, providing
477 discharge feeding flow in the lower macropore.

478 Late in the experiment a large saturated zone between 90-110 mm depth is apparent (i.e., large red
479 area in lower third of the column in Fig. 7i). While this view suggests the presence of a large void,
480 the feature is actually the consequence of the projection of the vertical slice of the CT image
481 intersecting the steeply dipping macropore. Thus, this feature simply represents the area where the
482 image slice happens to be contained fully within the crack forming the macropore. The water film
483 reaches the intersection of the upper macropore surface and the image slice after about 5.5 hours
484 in Figure 7e. Given that the image is a vertical slice of the column, after the initial film front passes
485 by, the zone of saturation within the macropore should remain constant if the film is of constant
486 thickness. In contrast, the macropore appears to fill from the top surface downward continuously
487 over time between 5.5-8hrs (Figs. 7e-i), suggesting that the film thickness along the top of the
488 macropore is increasing over this time. Concurrently, flow also appears to arrive in this region as
489 a thin film along the lower face of the macropore about 7 hours into the experiment (Fig. 7g). At
490 this point the applied flow rate was increased to 0.33 mL/min and both films thicken to the point
491 where they meet to form a capillary bridge (Fig 7h). At the end of the experiment (i.e. 8 hours),
492 the macropores filled to saturation (as water could not escape through the bottom plate of the
493 column) resulting in ponding at the soil surface (Fig. 7i).

494 Thus, over the course of the experiment a complicated series of behaviors can be seen involving
495 film flow, imbibition to the matrix, capillary bridging, and involvement of both macropores and
496 the matrix together forming flow networks within the soil. At low flow rates, film flow and lower
497 imbibition rates into the matrix appear to dominate. When the influent flow rate is increased,
498 imbibition rates to the matrix increase and films may thicken to the point of saturating the
499 macropore. Detailed examples for the occurrence of film flow, capillary bridging, and the
500 formation of flow networks are discussed below.
501

502 **3.3.2 Visualization of Macropore Flow Mechanisms**

503 **3.3.2.1 Film Flow in Macropores and Water transfer in Matrix**

504 At low saturations water can form thin films on the wall of a macropore, which is likely a primary
505 pathway for preferential flow in soils (Bouma & Dekker, 1978; Dragila & Wheatcraft, 2001;
506 Tokunaga & Wan, 1997). The development of film flow along the wall of a macropore is clearly
507 shown in Figure 8. Four hours into the experiment, a thin film is observed to be forming on the

right-hand side of macropore M3. The film appears to initiate from a wetted zone in the matrix at the top of the macropore. By 5 hours, the film is well established along the length of the macropore but is much thinner than the width of the macropore. It is notable that no change in water content adjacent to the macropore is observed up to this time in the experiment. Changes in the average film thickness are observed after this point. The film thickness grew over time and, when the flow rate was increased at 7 hours into the experiment, it exceeded 1 mm. Dragila and Wheatcraft (2001) indicate that a film thickness of greater than 1 mm shifts the flow regime from laminar to turbulent.

The conceptual model of film flow proposed by Tokunaga and Wan (1997) suggests imbibition of water into the matrix occurs along macropore surfaces. This conceptual model is supported qualitatively by Figure 8 and quantitatively by Figure 9, where the average volumetric water

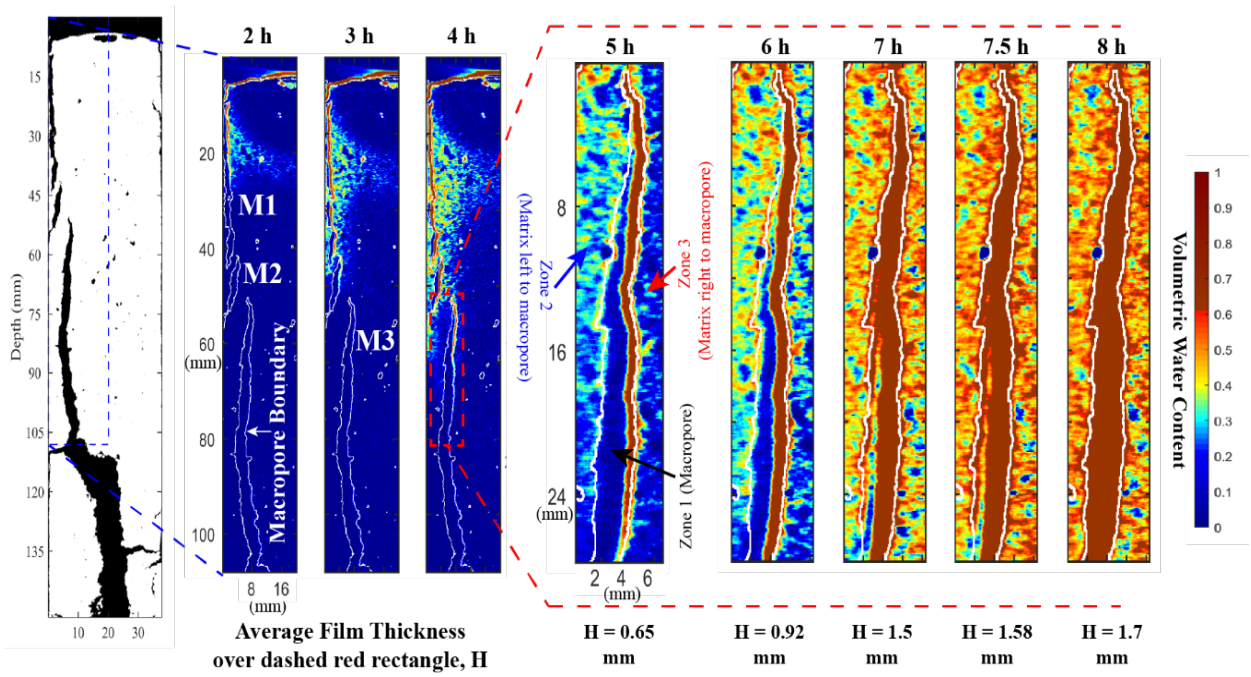

Figure 8. Visualization of thin film formation on a macropore surface (a white boundary indicates the wall of the macropore).

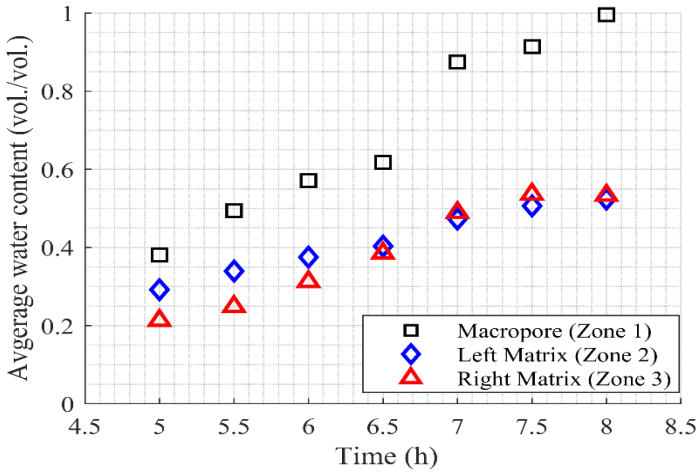

Figure 9. Average volumetric water content with time in three zones shown in Figure 8.

554 content is shown for three zones: zone 1 is macropore M3, zone 2 is the soil matrix to the left of
555 M3, and zone 3 is the soil matrix to the right of M3. Initially, the average water content in zone 2
556 is almost 10% (vol./vol.) higher than that in zone 3 (Fig. 9). As film flow is established along the
557 right side of macropore M3, the average water content in zone 3 increases and appears to
558 eventually surpasses that in zone 2 – we note, however, that the difference between the water
559 content in these zones at the end of the experiment is within the 5% (vol./vol.) error discussed
560 earlier and thus not definitive. The faster rate of water content increase in zone 3 relative to zone
561 2 is, however, consistent with imbibition occurring from the macropore to the matrix, though it is
562 difficult to discriminate changes in matrix water content caused by imbibition from the macropore
563 versus wetting of the matrix due to other matrix flow processes.

564 Despite the faster increase in water content over time in zone 3 versus zone 2, the average water
565 content in zone 2 also increases considerably over time, by almost 20% (vol./vol.), and both zones
566 appear to near saturation around 7 hours into the experiment. By this same time, film flow is also
567 observed to have initiated along the left side of the macropore. The films on both sides of the
568 macropore grow in thickness until eventually capillary bridging behavior can be observed and the
569 macropore is filled. The fact that the water content in zone 2 increases prior to the initiation of film
570 flow suggests that the source of water to this side of the macropore is from matrix flow, rather than
571 imbibition from the macropore. If this is indeed the case, it demonstrates that imbibition could be
572 occurring within one portion of a macropore (i.e., at the interface to zone 3) while at the same time
573 discharge from the matrix to the macropore could be occurring along another face (i.e., zone 2). It
574 is notable that macropore M3 is not directly connected to macropores higher in the column, thus
575 the water feeding the growth of films and imbibition to the matrix originates as flow from the
576 matrix above the macropore.

577 **3.3.2.2 Establishment of Flow Networks**

578 In this study, infiltration initially fed flow to the macropores from the top of the soil column and
579 water transfer from macropores to matrix was dominant. However, some macropores that are
580 disconnected from those where flow initially occurred are apparent in the column (e.g., M2 and
581 M3 in Fig. 4c and Fig. 8). In this case, water would need to transfer from a macropore with active
582 flow to the soil matrix, flow through the matrix, and then be discharged to the lower, disconnected
583 macropore. This final step requires that the water pressure in the matrix at the interface to the
584 macropore exceeds the 'water-entry' pressure of the macropore (Jarvis, 2007). In practice this
585 means that water contents in the matrix would need to approach saturation before flow could
586 initiate in the receiving macropore. Such behavior leading to the formation of a complex flow
587 network between macropores and the matrix is shown in Figure 10 for macropores M1, M2, and
588 M3, which were identified in Figure 4c and 8.

589 Images of the time-lapse water content distribution of four closely-spaced cross-sections (A, B, C
590 and D in Fig. 10) illustrate the formation of a flow network. The cross-sections from 3 hours into
591 the experiment (Fig.10 A1, B1, C1, D1) show that film flow occurs along one surface of macropore
592 M1 to the depth of cross-section A (i.e, A1), but no flow occurs in the other macropores. Some
593 imbibition appears to occur from M1 into the adjacent matrix. In addition, a wetted portion of the
594 matrix appears to occur next to macropore M2 (i.e., B1) and between macropore M2 and M3 (i.e.,
595 C1). Half an hour later, the film in M1 has reached cross section C. Additionally, water is now
596 present along one edge of M2, though the matrix immediatley adjacent to the macropore appears

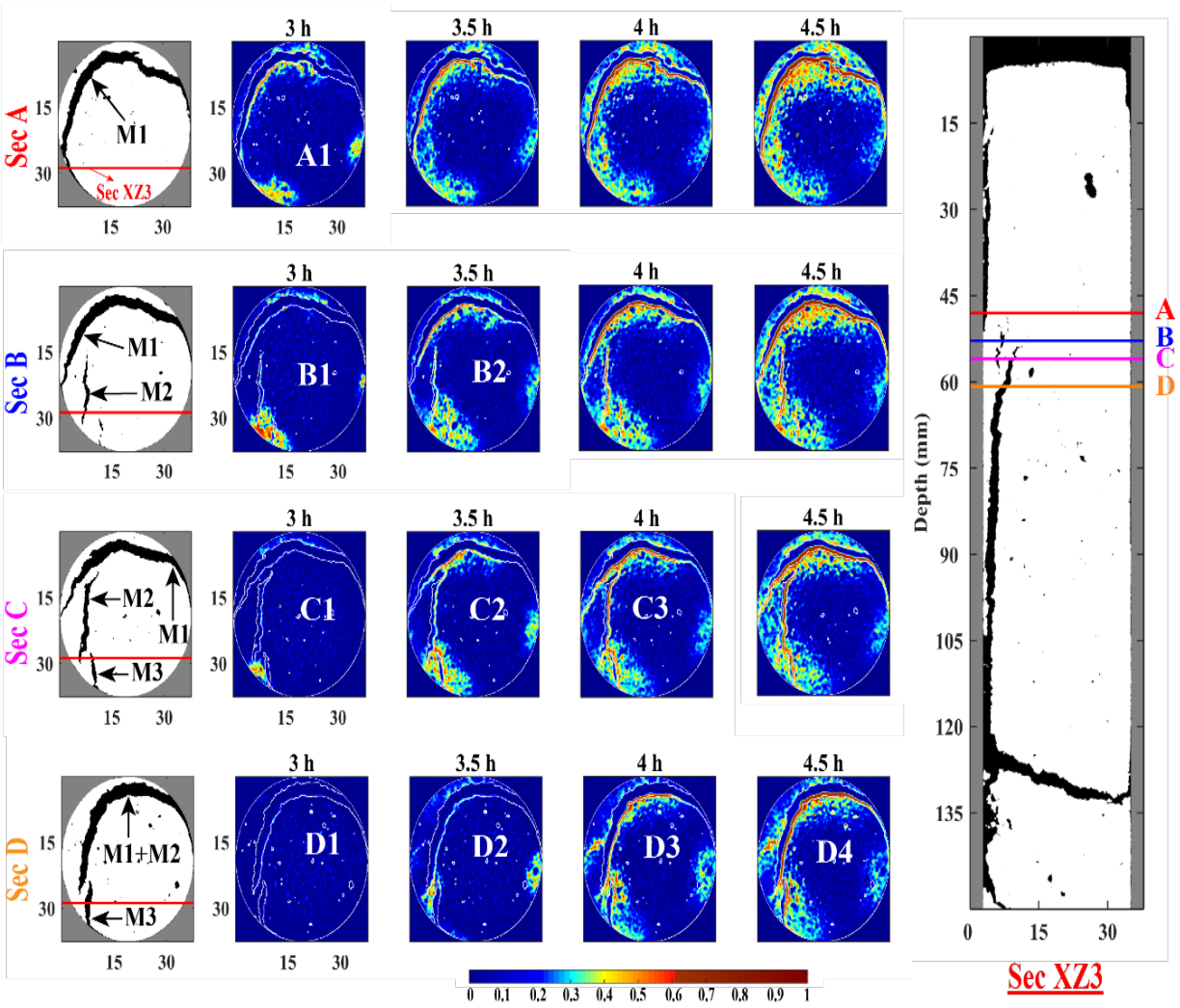

Figure 10. Macropore activation and matrix flow as connectors to macropores through time and space

to be dry in the central portion of the column. At this time M3 remains empty and without flow. The water content in the matrix between M2 and M3, however, is increasing (C2 and D2). Film flow is well established in M2 and may initiate in M3 within 4 hours from the start of the experiment (C3 and D3). The region between M2 and M3, as well as the area adjacent to M3 has wetted significantly (D3). At this time a small region of the matrix immediately between M1 and M2 is also very wet, suggesting that it may potentially act to connect these two macropores (C3). By 4.5 hours all three macropores are active with wetted regions between them. Though the exact mechanisms of interaction contributing to the establishment of this flow network cannot be inferred from the data, it is clear that both flow in the macropores and matrix contribute.

3.3.2.3 Capillary Bridging

When the flow rate is increased to a higher value causing the flow regime to shift from laminar to turbulent, 'capillary bridging' (i.e., a point of connection between the surfaces two liquids) might

occur at the narrowest sections of a variable-width macropore (Bouma & Dekker, 1978; Wang & Narasimhan, 1985). In addition, according to Ghezzehei and Or, 2005, flow with Re>3 requires faster velocities and, therefore, thicker films could break up into drops and bridges.

The capillary bridging phenomenon was seen in this study after the flow rate was increased to its maximum value 7 hours into the experiment (Fig. 11). Before increasing the flow to 0.33 mL/min (i.e., before 7 hours), flow was dominated by a film along one wall of the macropore in Figure 11. When the flow rate was increased, films also formed on the opposite wall of the macropore and eventually the two films touched to form capillary bridges that are clearly apparent in the images from 7.5 hours into the experiment. It is notable that the bridges appear to occur at locations where the soil protrudes into the macropore, apparently at a location where the formation of the crack was not uniform based on the shapes of the macropore surfaces.

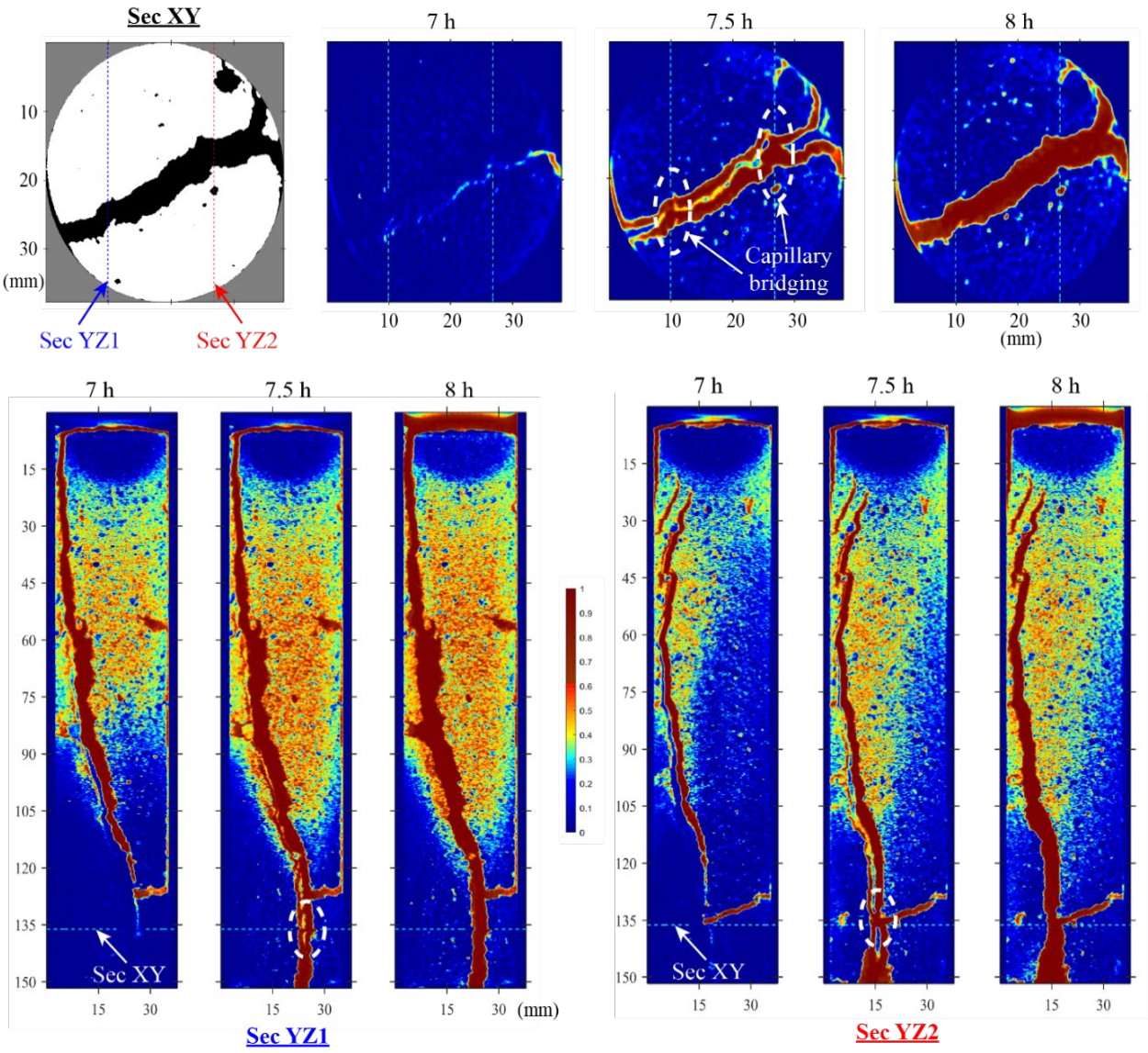

Figure 11. Capillary bridging formed by connected films along opposite macropore walls (i.e., XY is the cross-section and YZ1, YZ2 are longitudinal sections)

3.4 Comparison of the flow behaviour between the homogenous and macroporous columns

The average 1D volumetric water content profile from both experiments are compared in Figure 12. The curves are plotted as a function of cumulative flow volume rather than time, because the applied flow rates differed over time for the two columns. After a cumulative flow volume of approximately 26 mL, the wetting front of the laterally averaged volumetric water content profile is deeper in the macroporous soil than the non-macroporous soil. Despite the fast flow and clear zones of matrix bypass (i.e., low water content), the average water content in most of the macroporous column is high, illustrating significant transfer of water from macropore to matrix.

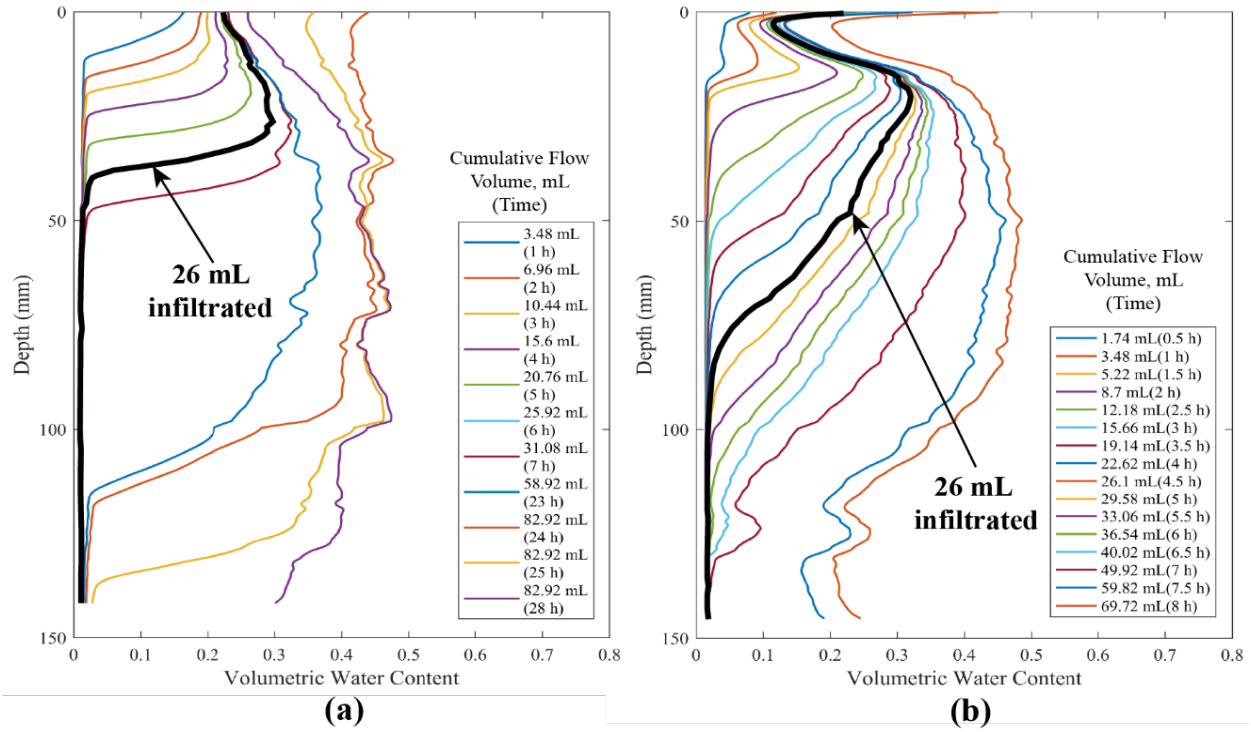

Figure 12. Averaged 1D water content profile with depth: (a) Non-macroporous column, (b) Macroporous column

4 Discussion:

The examples described above illustrate how the time lapse 4D CT data can provide insight to flow processes occurring in macroporous soils. While the non-macroporous column showed nearly uniform flow behavior, the soil containing desiccation cracks exhibited complex flow patterns within the macropores and between the macropores and soil matrix. The overall flow in the heterogeneous column was dominated by the macropores as water flowed across the soil to the edges of the column, where the macropores terminated at the soil surface. When the water supply was limited under a low applied infiltration rate, film flow occurred along one or more surface of the macropores. At higher flow rates the macropores were filled with water, often following capillary bridging events when films on opposite sides of a macropore intersected. This dynamic behavior of the macropores under different flow rates is not surprising, but it does suggest that which macropores are active or inactive at any moment in time during a flow event is not directly linked to macropore size. The initial activation of film flow was sometimes observed to occur near

717 the termination of a macropore where the walls of a crack converged to a corner. Thus, the detailed
718 geometry of a macropore and pore sizes in the adjacent matrix may play a role in initiating flow
719 in macropores.

720 Interactions between macropores and the soil matrix were also found to be important in the
721 experiment as it is clear that these processes are essential to forming a flow network in the soil.
722 The data support the conceptual model of film flow discussed by Tokunaga and Wan (1997),
723 suggesting that water can imbibe from a macropore to the matrix. This transfer process is important
724 for delivering water to storage deep within the soil profile, thus has important implications for
725 applications ranging from agriculture to biogeochemistry. The imbibition rate appeared to increase
726 in relation to film thickness, but further evaluation of these results is required to confirm this
727 finding. The results also suggest that the matrix can act as a source of water to a macropore. While
728 this idea is not new (e.g., Hendrickx & Flury, 2001), it is notable that a single macropore can
729 apparently perform different simultaneous functions within a soil. For example, the results suggest
730 that a film on one wall of a macropore may be transferring water to the soil matrix, whereas a
731 water film on the opposite wall may be fed by the matrix. Though our measurements are not
732 capable of explicitly delineating flow direction, the observed changes in water content of the
733 matrix adjacent to the macropores over time support this finding. The importance of such a
734 phenomenon on the net flow in soils is likely to be more important for soils with planar
735 macropores, such as the desiccation cracks in this study, versus tubular macropores produced by
736 worm burrows or root channels.

737 The specially designed vertically oriented CT scanner used in this study allowed for near real-time
738 monitoring of infiltration and does not require any kind of thresholding technique to obtain spatial
739 volumetric water content distribution over time. The use of a highly concentrated NaI solution
740 (1M) as tracer allowed for the clear visualization of flow patterns in the soil with the CT scanner,
741 but may have contributed to some shielding effects in the CT data and produced density driven
742 flow, which we neglected. Noise reduction and calibrating the NaI intensity was necessary for
743 better visualization of the flow patterns in the soils and for obtaining the water content estimates.
744 The non-macroporous column was not exactly homogeneous as there was layering inside the
745 column induced by the Proctor packing method, although the flow pattern was approximately
746 uniform throughout as expected in the case of a homogeneous column. The model (i.e., Eq. 4)
747 underestimated the water content calculated from CT images up to 10% (vol./vol.), though
748 accounting for shielding effects reduced this error significantly.

749 **5 Summary and Conclusion:**

750 This work illustrated that a modified preclinical CT imaging is an effective tool for fast (<8 minute
751 repeat time) and quantitative time-lapse monitoring of macropore-matrix flow mechanisms at the
752 pore scale. Many different types of flow phenomena were observed as a result of macropore-matrix
753 interactions, including, film flow, capillary bridging, macropore activation, imbibition, and the
754 formation of flow networks between macropores and the soil matrix. Preferential flow pathways
755 in the macroporous soil consist of a complex network of macropores, none of which were
756 continuous from the top to the bottom of the soil column. The soil matrix between two adjacent,
757 but discontinuous macropores appeared to act as a connection point to form deep and continuous
758 preferential flow paths through the soil. As a result of the interaction between macropores and the
759 matrix, much deeper infiltration of water is possible compared to an equivalent non-macroporous

soil. Wetting patterns also suggest that a substantial amount of lateral flow is supported by the macropores to wet the soil at depth. This enhanced flow has important consequences for fate and transport processes, particularly for the delivery of nutrients, contaminants and reagents like oxygen to deep within the soil profile. Also, in future, both quantitative and qualitative insight regarding the exchange of water between macropore and matrix could be obtained by comparing this experimental results with numerical modeling performed by coupling the Darcy–Richards equation in the matrix domain to the propagation of a kinematic dispersive wave in the macroporous domain or as already suggested a coupled model with free-surface flow (Di Pietro, Ruy, & Capowiez, 2003; Nimmo, 2010).

Acknowledgments

This material is based upon work supported by the U.S. Department of Energy Office of Science, Office of Basic Energy Sciences and Office of Biological and Environmental Research under Award Number DE-SC-00012530.

The experimental data in this manuscript will be provided access through ESS-DIVE (https://ess-dive.lbl.gov/) upon acceptance.

Reference

Abràmoff, M. D., Magalhães, P. J., & Ram, S. J. (2004). Image processing with imageJ. *Biophotonics International*. https://doi.org/10.1201/9781420005615.ax4

Barrett, J. F., & Keat, N. (2004). Artifacts in CT: Recognition and Avoidance. In *RadioGraphics* (Vol. 24). https://doi.org/10.1148/rg.246045065

Beven, K, & Germann, P. F. (1982). Macropores and water flows in soils. *Wat. Resour. Res.*, *18*(5), 1311–1325. https://doi.org/10.1029/WR018i005p01311

Beven, Keith, & Germann, P. (2013). Macropores and water flow in soils revisited. *Water Resources Research*, *49*(6), 3071–3092. https://doi.org/10.1002/wrcr.20156

Binley, A., Hubbard, S. S., Huisman, J. A., Revil, A., Robinson, D. A., Singha, K., & Slater, L. D. (2015). The emergence of hydrogeophysics for improved understanding of subsurface processes over multiple scales. *Water Resources Research*, *51*, 3837–3866. https://doi.org/10.1002/2015WR017016

Bouma, J., & Dekker, L. W. (1978). a Case Study on Infiltration Into Dry Clay Soil. *Adsorption Journal Of The International Adsorption Society*, *20*, 27–40. Retrieved from http://www.archive.org/details/plantrelationsfi00coul

Bouma, J., Jongerius, A., Boersma, O., Jager, A., & Schoonderbeek, D. (1977). The Function of Different Types of Macropores During Saturated Flow through Four Swelling Soil Horizons1. *Soil Science Society of America Journal*, *41*(5), 945–950. https://doi.org/10.2136/sssaj1977.03615995004100050028x

Capowiez, Y., Sammartino, S., & Michel, E. (2014). Burrow systems of endogeic earthworms:

Effects of earthworm abundance and consequences for soil water infiltration. *Pedobiologia*, *57*(4–6), 303–309. https://doi.org/10.1016/j.pedobi.2014.04.001

Clausnitzer, V., & Hopmans, J. W. (2000). Pore-scale measurement of solute breakthrough using microfocus X-ray computed tomography. *Water Resources Research*, *36*(8), 2067–2079.

Di Pietro, L., Ruy, S., & Capowiez, Y. (2003). Predicting preferential water flow in soils by traveling-dispersive waves. *Journal of Hydrology*, *278*(1–4), 64–75. https://doi.org/10.1016/S0022-1694(03)00124-0

Dogan, M., Moysey, S. M. J., Ramakers, R. M., Devol, T. A., Beekman, F. J., Groen, H. C., & Powell, B. A. (2017). High-Resolution 4D Preclinical Single-Photon Emission Computed Tomography/X-ray Computed Tomography Imaging of Technetium Transport within a Heterogeneous Porous Media. *Environmental Science and Technology*, *51*(5). https://doi.org/10.1021/acs.est.6b04172

Dragila, M. I., & Weisbrod, N. (2004). Fluid motion through an unsaturated fracture junction. *Water Resources Research*, *40*(2). https://doi.org/10.1029/2003WR002588

Dragila, M. I., & Wheatcraft, S. W. (2001). Free-Surface Films. In *Conceptual Models of Flow and Transport in the Fractured Vadose Zone* (pp. 217–242). https://doi.org/https://doi.org/10.17226/10102

Flury, M., & Wai, N. N. (2003). Dyes as tracers for vadose zone hydrology. *Reviews of Geophysics*, *41*(1), 1002. https://doi.org/10.1029/2001RG000109

Gantzer, C. J., & Anderson, S. H. (2002). Computed tomographic measurement of macroporosity in chisel-disk and no-tillage seedbeds. *Soil and Tillage Research*, *64*(1–2), 101–111. https://doi.org/10.1016/S0167-1987(01)00248-3

Germann, P. F., Smith, M. S., & Thomas, G. W. (1987). Kinematic wave approximation to the transport of Escherichia coli in the vadose zone. *Water Resources Research*, *23*(7), 1281–1287. https://doi.org/10.1029/WR023i007p01281

Ghezzehei, T. A., & Or, D. (2005). Liquid fragmentation and intermittent flow regimes in unsaturated fractured media. *Water Resources Research*, *41*(12), 1–10. https://doi.org/10.1029/2004WR003834

Gjettermann, B., Hansen, H. C. B., Jensen, H. E., & Hansen, S. (2004). Transport of Phosphate through Artificial Macropores during Film and Pulse Flow. *Journal of Environment Quality*, *33*(6), 2263–2271. https://doi.org/10.2134/jeq2004.2263

Hangen, E., Gerke, H. H., Schaaf, W., & Hüttl, R. F. (2005). Assessment of preferential flow processes in a forest-reclaimed lignitic mine soil by multicell sampling of drainage water and three tracers. *Journal of Hydrology*, *303*(1–4), 16–37. https://doi.org/10.1016/j.jhydrol.2004.07.009

Hendrickx, J. M. H., & Flury, M. (2001). Uniform and preferential flow mechanisms in the

vadose zone. *Conceptual Models of Flow and Transport in the Fractured Vadose Zone.Natl.Acad.Press, Washington, DC*, 149–187. https://doi.org/10.17226/10102

Iqbal, M. Z. (1999). Role of macropores in solute transport under ponded water condition produced by laboratory simulated intense storms. *Ground Water*, *37*(5), 674–681. https://doi.org/10.1111/j.1745-6584.1999.tb01159.x

Jarvis, N. J. (2007). A review of non-equilibrium water flow and solute transport in soil macropores: Principles, controlling factors and consequences for water quality. *European Journal of Soil Science*, *58*(3), 523–546. https://doi.org/10.1111/j.1365-2389.2007.00915.x

Jarvis, N., Koestel, J., & Larsbo, M. (2016). Understanding Preferential Flow in the Vadose Zone: Recent Advances and Future Prospects. *Vadose Zone Journal*, *15*(12). https://doi.org/10.2136/vzj2016.09.0075

Kalender, W. A. (2005). CT: The unexpected evolution of an imaging modality. *European Radiology, Supplement*, *15*(4), 21–24. https://doi.org/10.1007/s10406-005-0128-3

Ketcham, R. A., & Carlson, W. D. (2001). Acquisition, optimization and interpretation of x-ray computed tomographic imagery: Applications to the geosciences. *Computers and Geosciences*, *27*(4), 381–400. https://doi.org/10.1016/S0098-3004(00)00116-3

Koestel, J., & Larsbo, M. (2014). Imaging and quantification of preferential solute transport in soil macropores. *Water Resources Research*, *50*, 4357–4378. https://doi.org/10.1002/2014WR015351

Luo, L., & Lin, H. (2009). Lacunarity and Fractal Analyses of Soil Macropores and Preferential Transport Using Micro-X-Ray Computed Tomography. *Vadose Zone Journal*, *8*(1), 233–241. https://doi.org/10.2136/vzj2008.0010

Luo, L., Lin, H., & Halleck, P. (2008). Quantifying Soil Structure and Preferential Flow in Intact Soil Using X-ray Computed Tomography. *Soil Sci Soc Am J*, *72*(4), 1058–1069. https://doi.org/10.2136/sssaj2007.0179

Mees, F., Swennen, R., Geet, M. Van, & Jacobs, P. (2003). Applications of X-ray computed tomography in the geosciences. *Geological Society, London, Special Publications*, *215*(1), 1–6. https://doi.org/10.1144/gsl.sp.2003.215.01.01

Mooney, S. (2002). Three-dimensional visualization and quantification of soil macroporosity and water flow patterns using computed tomography. *Soil Use and Management*, *18*(2), 142–151. https://doi.org/10.1079/SUM2002121

Nimmo, J. R. (2010). Theory for Source-Responsive and Free-Surface Film Modeling of Unsaturated Flow. *Vadose Zone Journal*, *9*(2), 295. https://doi.org/10.2136/vzj2009.0085

Perret, J., Prasher, S. O., Kantzas, A., & Langford, C. (1999). Three-Dimensional Quantification of Macropore Networks in Undisturbed Soil Cores. *Soil Science Society of America Journal*, *63*(6), 1530–1543. https://doi.org/10.2136/sssaj1999.6361530x

Sammartino, S., Lissy, A.-S., Bogner, C., Van Den Bogaert, R., Capowiez, Y., Ruy, S., & Cornu, S. (2015). Identifying the Functional Macropore Network Related to Preferential Flow in Structured Soils. *Vadose Zone Journal*, *14*(10), 0. https://doi.org/10.2136/vzj2015.05.0070

Schmidt, J. P., & Lin, H. (2007). Water and bromide recovery in wick and pan lysimeters under conventional and zero tillage. *Communications in Soil Science and Plant Analysis*, *39*(1–2), 108–123. https://doi.org/10.1080/00103620701759053

Tippkötter, R., Eickhorst, T., Taubner, H., Gredner, B., & Rademaker, G. (2009). Detection of soil water in macropores of undisturbed soil using microfocus X-ray tube computerized tomography (µCT). *Soil and Tillage Research*, *105*(1), 12–20. https://doi.org/10.1016/j.still.2009.05.001

Tokunaga, T. K., & Wan, J. (1997). Water film flow along fracture surfaces of porous rock. *Water Resources Research*, *33*(6), 1287–1295. https://doi.org/10.1029/97WR00473

Tracy, S. R., Daly, K. R., Sturrock, C. J., Crout, N. M. J., Mooney, S. J., & Roose, T. (2015). Three-dimensional quantification of soil hydraulic properties using X-ray Computed Tomography and image-based modeling. *Water Resources Research*, *51*(2), 1006–1022. https://doi.org/10.1002/2014WR016020

Wang, J. S. Y., & Narasimhan, T. N. (1985). Hydrologic Mechanisms Governing Fluid Flow in a Partially Saturated, Fractured, Porous Medium. *Water Resources Research*, *21*(12), 1861–1874. https://doi.org/10.1029/WR021i012p01861

Warner, G. S., Nieber, J. L., Moore, I. D., & Geise, R. A. (1989). Characterizing Macropores in Soil by Computed Tomography. *Soil Science Society of America Journal*, *53*(3), 653–660. https://doi.org/10.2136/sssaj1989.03615995005300030001x

Weiler, M., & Naef, F. (2003). Simulating surface and subsurface initiation of macropore flow. *Journal of Hydrology*, *273*(1–4), 139–154. https://doi.org/10.1016/S0022-1694(02)00361-X

Weller, U., Leuther, F., Schlüter, S., & Vogel, H.-J. (2018). Quantitative analysis of water infiltration in soil cores using X-ray. *Vadose Zone Journal*, *17*(1). https://doi.org/10.2136/vzj2016.12.0136

Werth, C. J., Zhang, C., Brusseau, M. L., Oostrom, M., & Baumann, T. (2010). A review of non-invasive imaging methods and applications in contaminant hydrogeology research. *Journal of Contaminant Hydrology*, *113*(1–4), 1–24. https://doi.org/10.1016/j.jconhyd.2010.01.001